

Supplemental Information for:

Title: Determining Atomic-Scale Structure and Composition of Organo-Lead Halide Perovskites by Combining High-Resolution X-ray Absorption Spectroscopy and First-Principles Calculations

Author List: Walter S. Drisdell^{1*}, Linn Leppert^{2,3}, Carolin M. Sutter-Fella¹, Yufeng Liang², Yanbo Li¹, Quynh P. Ngo^{4,5}, Liwen F. Wan², Sheraz Gul^{1,6}, Thomas Kroll⁷, Dimosthenis Sokaras⁷, Ali Javey⁴, Junko Yano⁶, Jeffrey B. Neaton^{2,3,8}, Francesca M. Toma^{1*}, David Prendergast^{2*}, Ian D. Sharp^{1*}

¹Chemical Sciences Division, Lawrence Berkeley National Laboratory, Berkeley, CA 94720, USA.

²Molecular Foundry, Lawrence Berkeley National Laboratory, Berkeley, CA 94720, USA.

³Department of Physics, University of California, Berkeley, CA 94720, USA.

⁴Department of Electrical Engineering and Computer Sciences, University of California, Berkeley, CA 94720, USA.

⁵Materials Sciences Division, Lawrence Berkeley National Laboratory, Berkeley, CA 94720, USA.

⁶Molecular Biophysics and Integrated Biology Division, Lawrence Berkeley National Laboratory, Berkeley, CA 94720, USA.

⁷Stanford Synchrotron Radiation Lightsource (SSRL), SLAC National Accelerator Laboratory, Menlo Park, CA 94025, USA.

⁸Kavli Energy NanoScience Institute at Berkeley, Berkeley, CA 94720, USA.

* = corresponding author

Sample Preparation:

$\text{CH}_3\text{NH}_3\text{Pb}(\text{I}_{1-x}\text{Br}_x)_3$ films on FTO glass substrates were synthesized by solution processing. For that purpose, two precursor solutions with 1 M $\text{CH}_3\text{NH}_3\text{I}$ and 1 M PbI_2 (Alfa Aesar, 99.9985%), and 1 M $\text{CH}_3\text{NH}_3\text{Br}$ and 1 M PbBr_2 (Sigma-Aldrich 99.999%), respectively, were dissolved in DMF and filtered with a 0.2 μm polytetrafluorethylene filter. To obtain mixed halide films, the two precursor solutions were mixed in the desired volume ratio, for example a 50% Br-containing film was synthesized by mixing 50 vol% of the pure Iodine precursor with 50 vol% of the pure Bromide precursor. The mixed precursor solution as well as the FTO substrates were pre-heated at 110 °C on a hot plate before the precursor was spun onto the substrate at 500 / 2000 rpm for 5 / 45 s. The $\text{CH}_3\text{NH}_3\text{Pb}(\text{I}_{1-x}\text{Br}_x)_3$ films were dried on a hot plate at 110 °C under N_2 flow for 45 min. A protective PMMA layer was spin coated on the perovskite films before further characterization.

The film composition was extracted from energy dispersive X-ray spectroscopy measurements at 10 kV acceleration voltage on a FEI Quanta FEG 250 A summary of the samples and respective composition is given in Table S1. The samples did not show any PbI_2 secondary phase as analyzed by X-ray diffraction measurements.

Table S1. Target halide composition and actual composition as extracted from EDX measurements.

Target	EDX
x	x
0	0
0.1	0.1
0.2	0.2
0.3	0.3
0.4	0.5
0.5	0.4
0.6	0.5
0.7	0.6
0.8	0.9
0.9	0.8
1	1

X-ray Absorption Spectroscopy (XAS):

i) Fluorescence yield XAS

Fluorescence yield XAS of $\text{CH}_3\text{NH}_3\text{PbX}_3$ (MAPbX_3 , $\text{X}=\text{I}, \text{Br}, \text{Cl}$) with various halide compositions was performed at the Pb L_I -edge, Pb L_III -edge, Br K-edge and I K-edge at beamline 4-1 at the Stanford Synchrotron Radiation Lightsource (SSRL) at SLAC National Accelerator Laboratory. X-ray energy was selected using a Si (220) double crystal monochromator, with a resolution ($\Delta E/E$) of 10^{-4} . The unfocused 4 x 18 mm beam was reduced to a 1 x 1 mm spot size using mechanical slits. Incoming X-ray intensity was monitored with an N_2 -filled ion chamber (for Pb L_I -edge, Pb L_III -edge, and Br K-edge) or Ar-filled ion chamber (for the I K-edge) before interaction with the samples. Fluorescence yield was detected at 90° with a 32-element Ge detector. Energy was calibrated to Pb foil for the Pb L_I -edge and Pb L_III -edge, PbBr_2 for the Br

K-edge, and elemental iodine for the I K-edge. Samples were placed in an N₂-purged box with kapton windows during measurement to avoid exposure to moisture. All spectra were subjected to a linear baseline correction and post-edge intensity normalization.

X-ray absorption spectra at the Pb L_I-edge, Br K-edge and I K-edge are shown in Figure S1. No significant changes are seen as a function of I/Br composition. At the Pb L_I-edge, an increase in intensity is seen for higher Br compositions, but no spectral shifts are observed. The Br K-edge spectra display small shifts and spectral broadening, but these show no trend with I/Br composition and may be due to monochromator drift.

ii) HERFD XAS

High energy resolution fluorescence detection (HERFD) XAS utilizes an emission spectrometer to isolate the peak of a single fluorescence line for detection.¹ This effectively monitors a diagonal slice across the resonant inelastic X-ray scattering (RIXS) plane, avoiding the majority of intrinsic lifetime broadening that manifests in axial directions.² As long as there are no significant contributions from off-diagonal features in the RIXS plane – there are none at the Pb L_{III}-edge³ – HERFD XAS offers a highly accurate approximation of the standard absorption spectrum with minimal broadening.² HERFD XAS was carried out at beamline 6-2 of the Stanford Synchrotron Radiation Lightsource (SSRL). A monochromatic incident beam was delivered through a liquid nitrogen cooled Si(311) double crystal monochromator, whereas two Rh-coated mirrors (at about 3.75 mrad), positioned before and after the monochromator, were used to collimate and focus the wiggler radiation and simultaneously suppress the higher order harmonics. The incident x-ray flux at the target position was estimated to be $\sim 4 \times 10^{12}$ photons/s and the beam size FWHM was measured to be $\sim 120 \times 400$ μm^2 (vertical x

horizontal). The x-ray fluorescence radiation was collected with a high energy resolution using a seven crystal Johann type spectrometer set on overlapping vertical Rowland circles of 1 m.⁴ Seven Si(880) crystals with 100 mm of diameter were aligned to the maxima of Pb-L β 5 emission line (13014.3 eV) and the energy resolution was measured to be ~1.5 eV. Spectra were collected in a grazing incidence geometry.

The higher photon flux for HERFD XAS, compared to fluorescence yield XAS, resulted in much faster beam damage upon extended exposure of perovskite samples to the X-ray beam. To mitigate this, samples were mounted inside a nitrogen-purged bag to minimize exposure to moisture; in combination with the PMMA coating discussed above, this served to slow beam-induced damage enough to allow collection of reliable spectra. Tests showed that two scans could be collected on a single sample spot before spectral changes indicative of beam damage began to appear (Figure S2). For the data reported here, only one scan per spot was used, moving the sample vertically between scans to access a fresh spot on the sample for each scan. Samples were highly uniform with identical spectral shapes at each spot. Typically 9 – 14 spots (dependent on exact sample size), 1 mm apart, were used for data collection on each sample, and the corresponding spectra were averaged. Before analysis a linear baseline was subtracted from each scan, and intensity was normalized to 1 in the post-edge region (13057.5 eV – 13170 eV).

iii) Linear combination fitting

Linear combination fitting was used to test if spectra of mixed-halide perovskites could be reproduced by combining the spectra for MAPbI₃ and MAPbBr₃. Fits were performed using the built in linear combination fitting function in the Athena data processing software package,⁵ using an energy range of 13018.9 eV – 13061.9 eV. An example fit to the spectrum for the

mixed-halide perovskite with a Br:I ratio of 0.4 is shown in Figure S3. This fit returns a Br:I ratio of 0.368, and fails to accurately reproduce the energy, intensity, or spectral shape of the rising edge and main edge spectral features. This confirms that the mixed-halide perovskites are not simply two-phase mixtures of MAPbI₃ and MAPbBr₃.

Spectral calculations:

Simulations of the Pb L3-edge absorption spectra are performed with the XCH approach,⁶⁻⁷ as implemented by a modified simulation package based on QuantumESPRESSO.⁸ The Pb core-hole effect is simulated with a pseudopotential generated for a Pb atom in which one 2p electron is removed. The perovskite structure with the core-excited Pb atom is then put into a supercell with a dimension larger than 9 Angstrom in each lattice direction, which is large enough to truncate the spurious interaction among periodic images of the core-excited atom. The projector-augmented wave (PAW) formalism⁹ is adopted to enable core-excitation transition amplitudes to be calculated using pseudopotentials. We employed Vanderbilt ultrasoft pseudopotentials¹⁰ with a plane-wave kinetic energy cutoff of 30 Ryd, sufficient for convergence the total energy and electronic structure of the self-consistent-field calculation. To produce the XAS spectra, we first converge the total charge density of the 9 Å³ supercell with a 2x2x2 k-grid for its Brillouin zone (BZ). Then we employ the Shirley interpolation scheme^{7, 11} to efficiently produce band energies and wavefunctions on a denser 5x5x5 k-grid. The final spectra are convoluted with a Gaussian broadening of 1.0 eV.

The relative energy alignment for the spectra is determined by calculating the equivalent of the formation energy for the core-excited Pb atom in different chemical environments. The method has been shown to reliably reproduce energy alignment for calculated spectra of ionic and covalent compounds.^{6, 9, 12-14} In light of possible high-order multipole effects in heavy-

element X-ray absorption, we have also included quadrupole transitions in calculating the Pb L_{III} -edge. Their contributions, however, turn out to be less than 0.1% of the dipole contribution and can be safely neglected.

When estimating the core level shifts in different chemical environments (e.g. the P1 – P5 structures), we use the full core hole (FCH) method, in which the photoexcited electron is not included (by contrast with the XCH method), and simply calculate total energy differences for these valence electronic systems including the presence of the core hole.

Final State Analysis:

A molecular orbital diagram depicting the energy ordering of the orbitals formed from Pb 6d and Br 4d atomic orbitals in a perfect $PbBr_6$ octahedron is shown in Figure S5. The ordering was calculated on a model $PbBr_6$ octahedron with a bond distance of 2.5 Å using the B3LYP functional¹⁵⁻¹⁸ with a specialized basis consisting of the LANL2DZ effective core potentials for Pb and Br.¹⁹⁻²⁰ Two sets of t_{2g} and e_g orbitals are formed, all of which are empty; the spectra probe the lower set, as the higher set lies in the high energy region of the spectrum which is dominated by scattering interactions. The XCH spectrum for $MAPbBr_3$ (P4) is shown in Figure S6, along with the spectral contributions from final states with individual Pb d character, showing general agreement with the ordering shown in Figure S5.

We have located relevant individual final states in the computed spectrum of $MAPbBr_3$, although much of the degeneracy is broken due to hybridization with the MA cations. Figure S7 shows the spectrum for $MAPbBr_3$ (P4) with individual electronic transitions marked. Transitions to similar states are circled, with final states for the transitions indicated in red pictured in panels a-f. Importantly, due to the presence of the MA cations, the d_{xz} and d_{yz} final states are oriented

away from the Pb-Br bonds in the xy plane. This is why the rising edge spectral feature, as well as the main edge spectral feature which is dominated by d_{z^2} final states, are especially sensitive to structural details in the apical direction (e.g. apical halide identity, Pb-X apical bond length, octahedral tilt along apical axis). We note that for cubic perovskite structures like MAPbBr₃, the apical direction is defined by the orientation of the MA cation; in the real system, we expect random MA orientations, but energetically each molecule will favor an orientation along one of the cardinal axes, defining a local apical direction. The energy barrier to rotation is predicted to be as small as 10 – 20 meV,²¹ however, so deviation from these orientations is expected and should broaden spectral features. But this is generally a smaller effect than thermal disorder of the PbX₆ octahedra; see the “Molecular Dynamics” section below for more details.

States oriented away from the apical direction appear at different energies. Mixed Pb d/p states are found in the pre-edge region near 13037 eV. States with Pb d_{xy} character tend to appear at higher energy than the d_{xz} and d_{yz} states in the rising edge region, due to hybridization with the MA cation. Most are in the 13041 – 13043 eV range, but some appear at much higher energy (Figure S7f). Similarly, the $d_{x^2-y^2}$ states are also shifted to higher energy than the d_{z^2} final states, again due to hybridization with MA (Figure S7e).

Structural computations:

Our mixed APbX₃ halide structures are computed using density functional theory (DFT) within the generalized-gradient approximation of Perdew, Burke, and Ernzerhof (PBE) and the projector augmented wave formalism (PAW)²²⁻²³ as implemented in VASP.²⁴⁻²⁵ To construct the systems with $x = 0.4$, $x = 0.6$ and $x = 0.8$, we start from supercells with 16 formula units corresponding to 19, 29 and 38 Br atoms, respectively, that are randomly distributed over the

available halide sites. The dipole moment of the MA cation induces polar distortions in the inorganic PbX_3 cage that we assume to be largely suppressed or averaged out at room and higher temperatures due to the rotational dynamics of the molecule.^{21, 26} We therefore replace MA cations by “pseudoatoms” in our relaxations of the super cells. This is done by using the virtual crystal approximation (VCA) mixing Rb and Cs at the A site.²⁷ We choose the mixing ratio such that after a full relaxation, the unit cell volume corresponds to the experimental volume.²⁸ The very good agreement with experiment demonstrated in Figure S10a is achieved because of a beneficial cancellation of errors: the well-known tendency of PBE to overestimate unit cell volumes and the slightly smaller A site volume of Cs and Rb as compared to MA. Importantly, this method allows us to fully relax all internal coordinates and the volume of the supercells without introducing artificial structural distortions due to choosing fixed orientations of the MA cations. Figure S10b shows the average Pb-X bond lengths of our relaxed pure and randomly mixed structures. Since there is no detailed structural information from experiments on mixed halide perovskites, we just note that the agreement with experiment is slightly better for the cubic MAPbBr_3 (space group: Pm-3m) than for MAPbI_3 (space group: I4/mcm). Static DFT structure optimizations of the latter tend to overestimate the rotation angle of the PbI_6 octahedra by $\sim 5\text{-}10^\circ$,²⁹ resulting in less accurate Pb-I bond lengths. Since XRD experiments show that mixed halide perovskites with $x=0.4$, $x=0.6$ and $x=0.8$ have Pm-3m symmetry this problem is not relevant here.

Since our simulations show that final state wavefunctions are sensitive to the choice of the A site cation (see “Cation Effects” below), in a final step we replace the pseudoatom by MA molecules again in an antiparallel arrangement (no net dipole) and relax the atomic positions of the molecules while keeping the rest of the structure fixed. For all relaxations we apply a

convergence criterion of 0.05 eV/Å on the forces. We use a plane wave energy cutoff of 500 eV, 4x4x4 k-point grids and PAW pseudopotentials with the following atomic configurations: N ($2s^2 2p^3$), C ($2s^2 2p^2$), Rb ($4s^2 4p^6 5s^1$), Cs ($5s^2 5p^6 6s^1$), Pb ($6s^2 6p^2$), I ($5s^2 5p^5$) and Br ($4s^2 4p^5$). Spin-orbit coupling effects are not included in our structural relaxations since they have been shown to introduce insignificant changes in structural parameters.³⁰

Cation Effects:

The “pseudoatom” structures revealed a sensitivity of the final state wavefunctions to the cation. To illustrate the effect of different cations on computed spectra, a direct comparison between computed XAS for MAPbI₃ and the same structure in which MA cations have been replaced with Cs is shown in Figure S11. The Cs introduces a blueshift of 1.1 eV in the rising edge feature, as well as a blueshift of 0.3 eV in the main edge feature. Core level shifts from FCH computations predict a redshift of 0.56 eV instead. Visualizing the final state wavefunctions for the two structures reveals that the d_{xz} and d_{z^2} orbitals, also shown in Figure S11, display clear interactions with the MA cations that are not present for Cs cations. The HERFD XAS are therefore sensitive to previously reported hydrogen bonding interactions between the MA cations and the PbI₆ cages.³¹ This interaction is strongest for the d_{xz} and d_{yz} rising edge states, consistent with the larger discrepancy in spectral position for the rising edge feature.

Molecular Dynamics:

To estimate the effects of thermal motion on our spectra, we have performed ab initio molecular dynamics simulations on MAPbBr₃ using VASP. To be consistent, we use the same parameter sets as in the structural relaxations except for the simulation size, where a supercell

with 24 formula units is used. The system was equilibrated at 300K using a Nosé thermostat at a time step of 0.25 fs and a production run of 1 ps was performed to compute the pair distribution function (PDF) and angular distribution function (ADF). Figure S13 shows a comparison of the PDF and ADF between an MD snapshot for MAPbBr₃ and the randomized structure for the $x = 0.6$ composition (MAPb(Br_{0.6}I_{0.4})₃). The ADF is computed for all nearest neighbor Pb-halide bond angles and the range related to the octahedral tilting is plotted in Figure S13. In static MAPbBr₃ (0K relaxation) where there is no octahedral tilting, the Pb-Br-Pb bond angles should be exactly 180°. Defining the octahedral tilting angle as a deviation from 180°, tilting angles as large as 30° are observed when room temperature thermal fluctuation is considered (blue line). The randomized structure for $x = 0.6$ displays tilting angles between ~4.5° and 36° (red line), a similar but slightly larger amplitude of tilting compared to the MD averaged MAPbBr₃ structure. The XCH spectrum calculated from an MD snapshot is shown in Figure S14, demonstrating that the MD has captured some of the thermal effects, producing a better match to the experimentally observed spectral broadening.

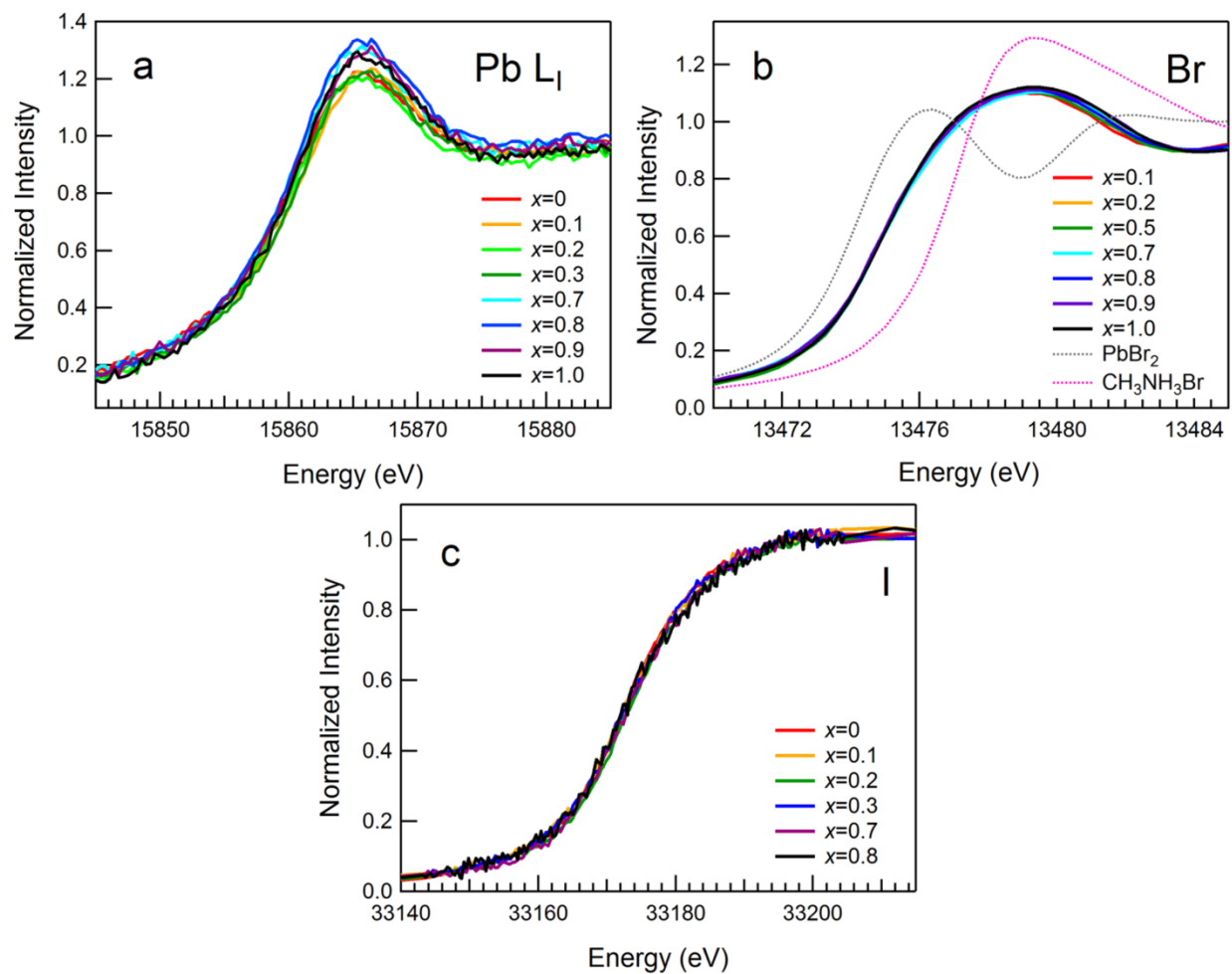


Figure S1: Fluorescence yield XAS. Fluorescence yield XAS of $\text{CH}_3\text{NH}_3(\text{I}_{1-x}\text{Br}_x)_3$, as a function of x , at the **a)** Pb L_1 -edge, **b)** Br K-edge and **c)** I K-edge. At the Br K-edge, reference spectra of PbBr_2 and $\text{CH}_3\text{NH}_3\text{Br}$ are shown for comparison.

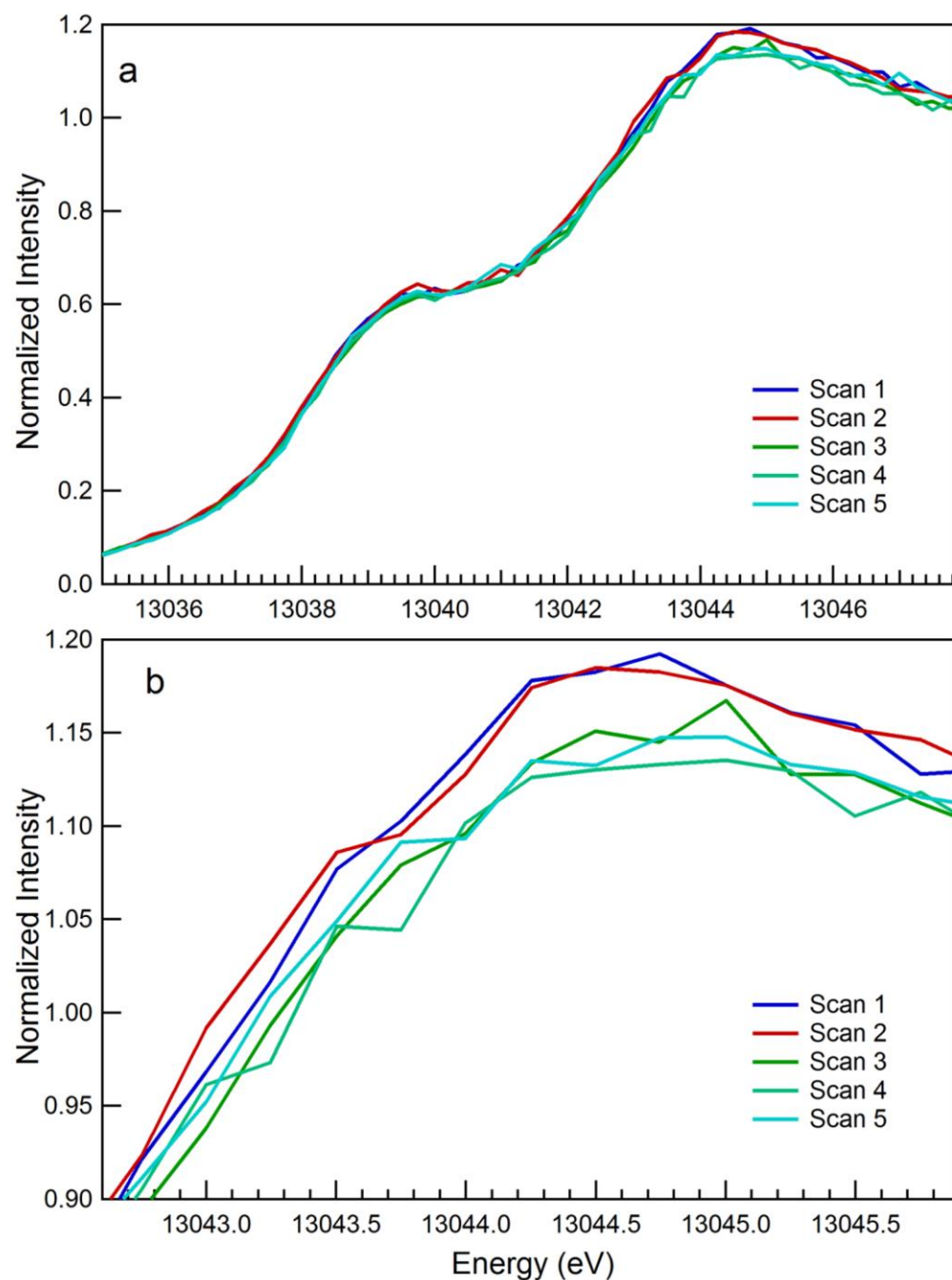


Figure S2: X-ray induced sample damage. (a) Repeated HERFD XAS scans of $\text{CH}_3\text{NH}_3\text{PbI}_3$ on the same sample spot. After the second scan, intensity loss in the main edge feature near 13044.5 eV characteristic of beam-induced sample damage begins to appear (accompanied by visible discoloration of sample). (b) A zoomed view of the main edge region highlighting the

spectral change. For the data in this study, only one scan per sample spot was used, for spots ~1 mm apart.

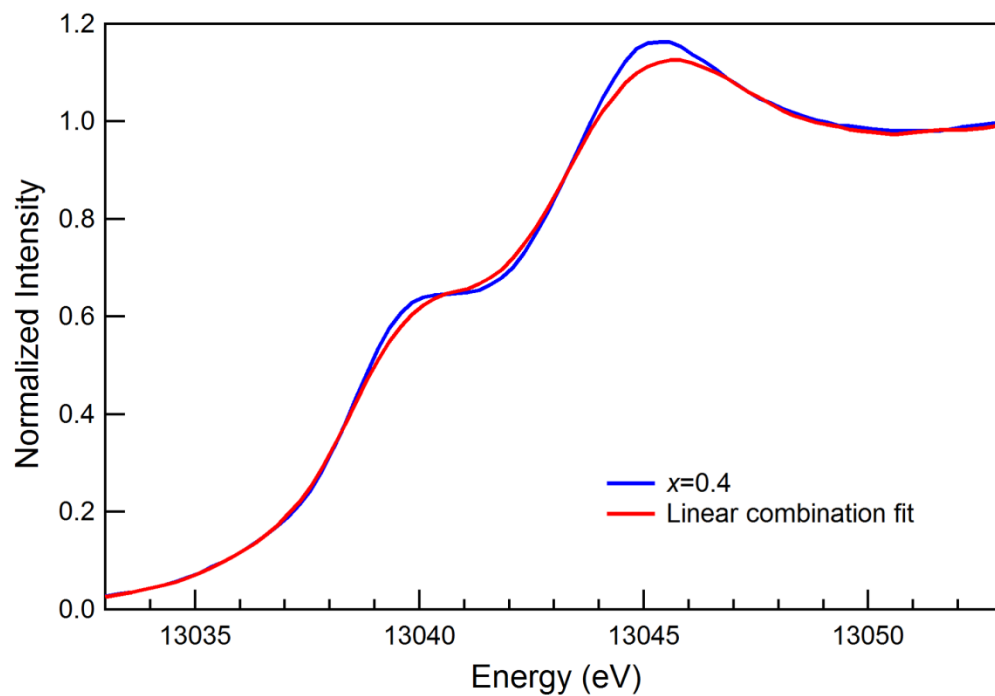


Figure S3: Linear combination fit. HERFD XAS spectrum for the mixed-halide perovskite with $x = 0.4$ (blue) and a linear combination fit using the spectra of MAPbI_3 and MAPbBr_3 (red). The fit returns an x of 0.368.

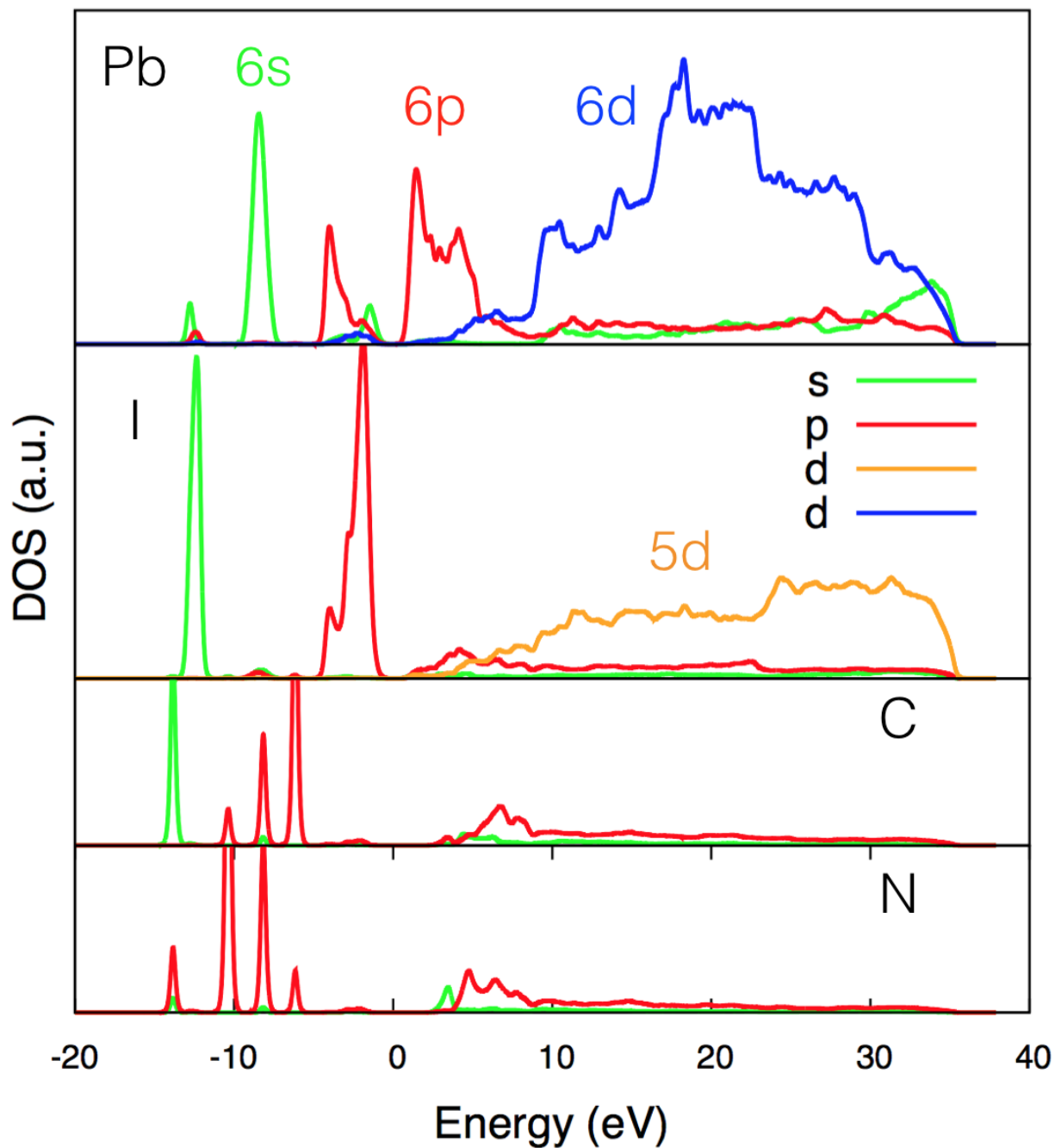


Figure S4: Density of states. Calculated density of states (DOS) for each element in MAPbI₃.

The Pb 6d states probed by the Pb L_{III}-edge HERFD XAS lie ~10 eV above the Fermi level, above the Pb 6p states that dominate the conduction band minimum.

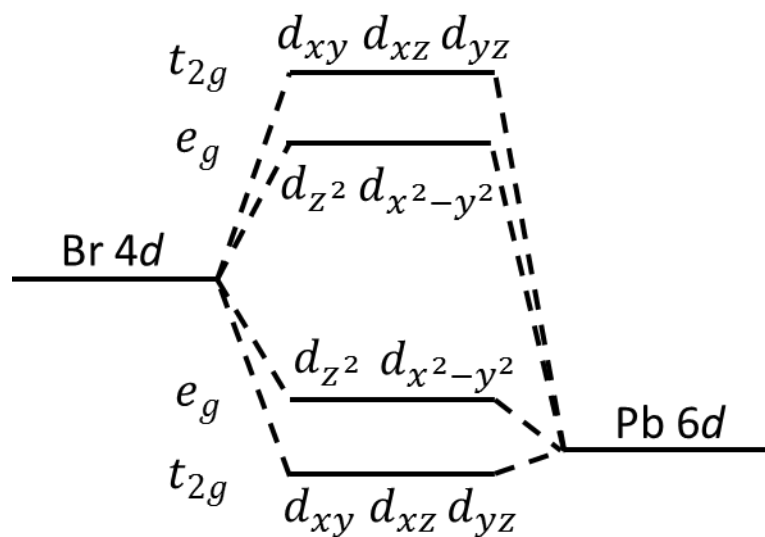


Figure S5: MO diagram for d-d mixing in octahedral symmetry. Diagram showing the energy ordering of the molecular orbitals formed in a perfect PbBr_6 octahedron with 2.4 Å bond length. The Pb d character of the resulting t_{2g} and e_g states is listed. The lower set of t_{2g} and e_g states are probed by HERFD XAS.

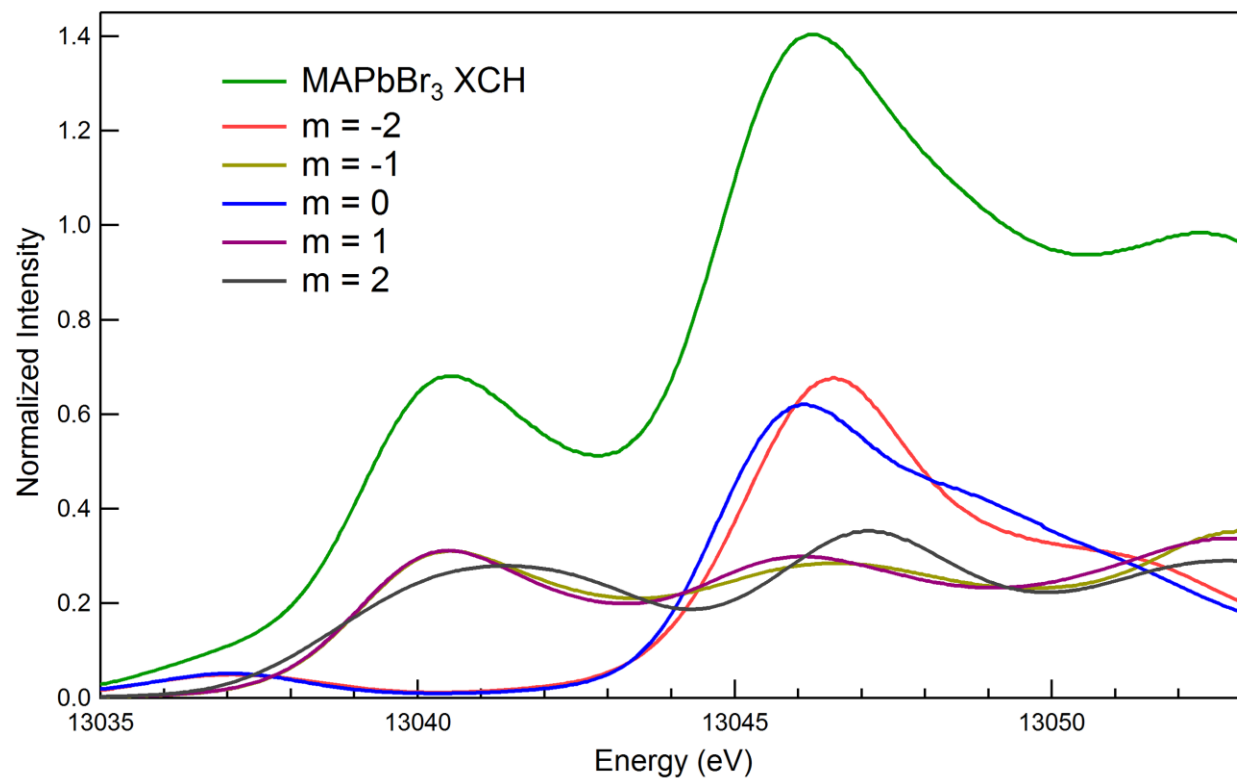


Figure S6: *d*-orbital contributions to spectrum. The calculated spectrum of MAPbBr₃, shown with individual contributions from final states with specific Pb *d* character. The rising edge feature is dominated by transitions to states with Pb d_{xy} , d_{xz} , and d_{yz} character, whereas the rising edge feature is dominated by transitions to states with Pb d_{z^2} and $d_{x^2-y^2}$ character. Some Pb d_{z^2} and $d_{x^2-y^2}$ character is observed in the pre-edge region near 13037 eV, due to hybridization with Pb *p* states (see Figure S7). The slight splitting between states with d_{xy} character versus d_{xz} and d_{yz} character, as well as the small splitting between states with d_{z^2} and $d_{x^2-y^2}$ character, are due to hybridization with MA (see Figure S7).

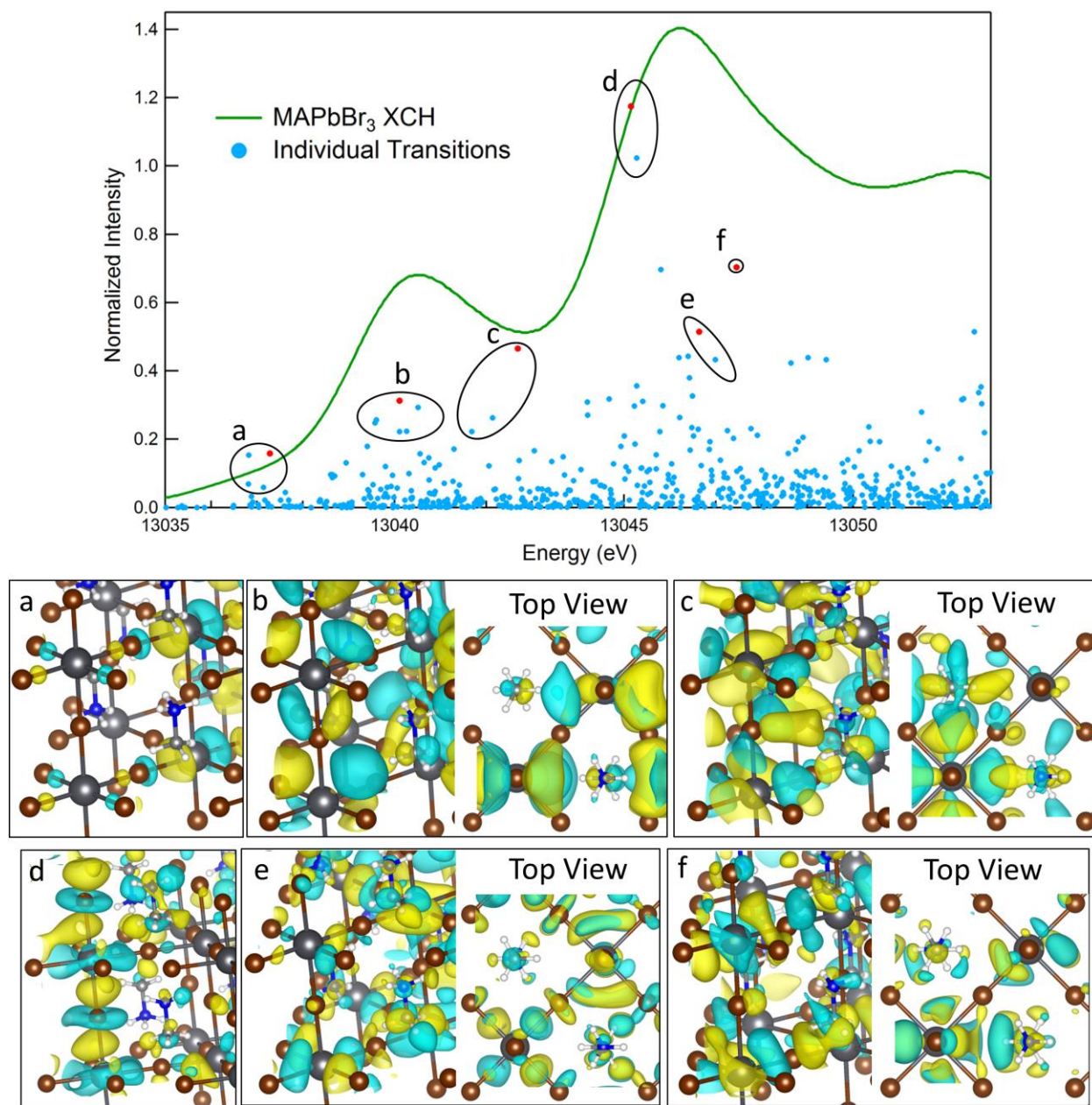


Figure S7: Final State Analysis for MAPbBr₃. Top panel: the computed spectrum for MAPbBr₃ (P4, green), plotted with the individual electronic transitions before broadening (blue). Transitions displaying different Pb *d* character are circled, with the final states for transitions indicated in red pictured in panels a-f. In all cases, including top views, the excited Pb atom is at the bottom left of the image. Pb are dark grey, Br are brown, C are light grey, N are blue, and H are white. The opposing phases of the orbitals are shown in yellow and cyan. Isosurfaces are set

to contain 40% of the electron density of each state. (a) $\text{Pb}(d/p)/\text{Br}(p)$ mixed states in the pre-edge region. (b) $\text{Pb}(d_{xz})/\text{Br}(d_{xz})$ (pictured) and $\text{Pb}(d_{yz})/\text{Br}(d_{yz})$ states in the rising edge. (c) $\text{Pb}(d_{xy})/\text{Br}(d_{xy})$ states showing hybridization with MA. (d) $\text{Pb}(d_{z^2})/\text{Br}(d_{z^2})$ states in the main edge. (e) $\text{Pb}(d_{x^2-y^2})/\text{Br}(d_{x^2-y^2})$ states in the main edge. (f) A $\text{Pb}(d_{xy})$ state hybridized to MA instead of Br.

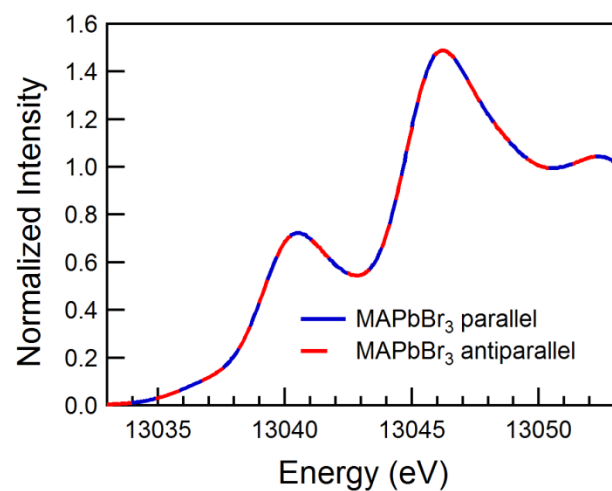


Figure S8: Orientation of MA. Computed XAS of MAPbBr₃ with parallel orientations for the MA cations (P4, blue), and antiparallel orientations for the MA cations (red); the spectra are identical.

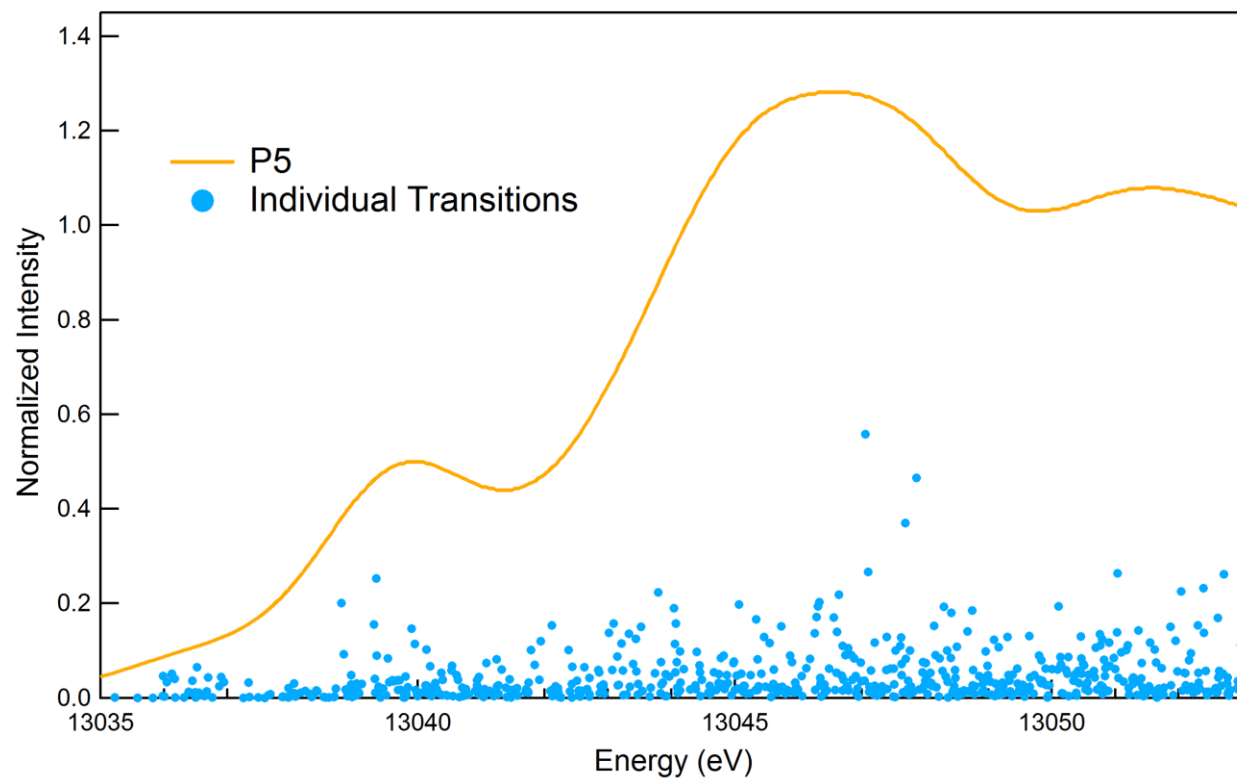


Figure S9: Individual transitions for the P5 structure. The strong $\text{Pb}(d_{z^2})/\text{Br}(d_{z^2})$ transitions seen in the main edge near 13045.5 eV for MAPbBr_3 (P4) no longer appear, as the octahedral tilts in P5 break the strong Pb-Br couplings. Instead, intensity is split among several lower intensity hybridized states, resulting in a broader and slightly blueshifted main edge peak in the spectrum.

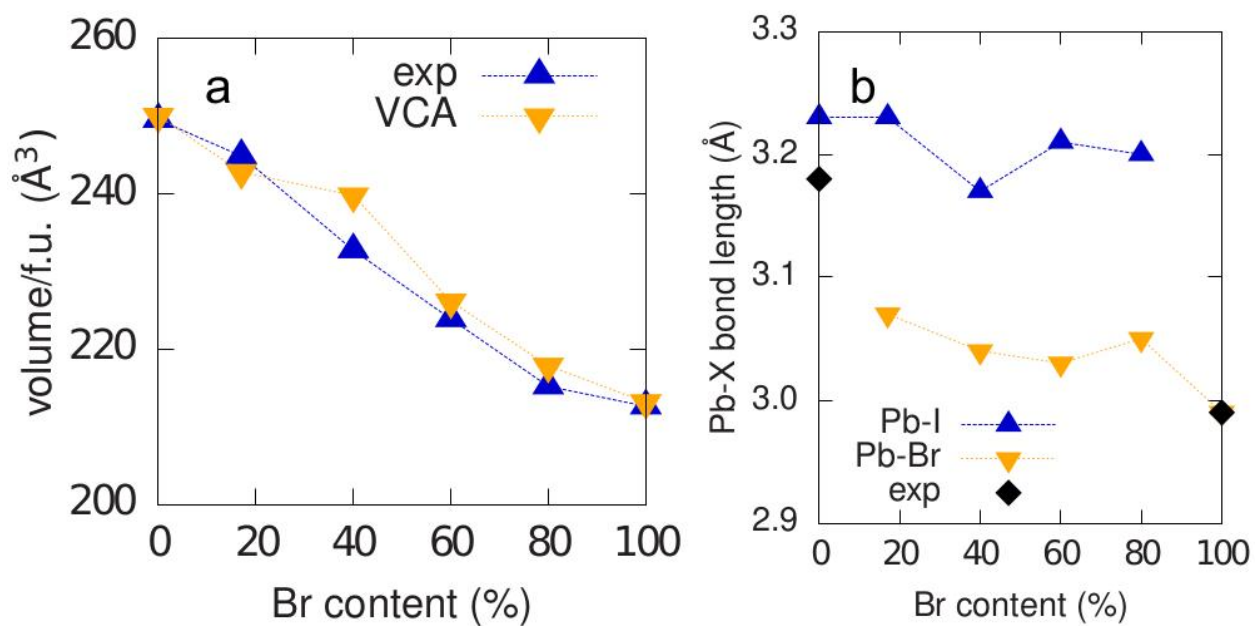


Figure S10: Pseudoatom structural parameters. Comparison between (a) experimental and computed lattice parameters, and (b) Pb-X bond lengths, as a function of Br content, using “pseudoatom” structures.

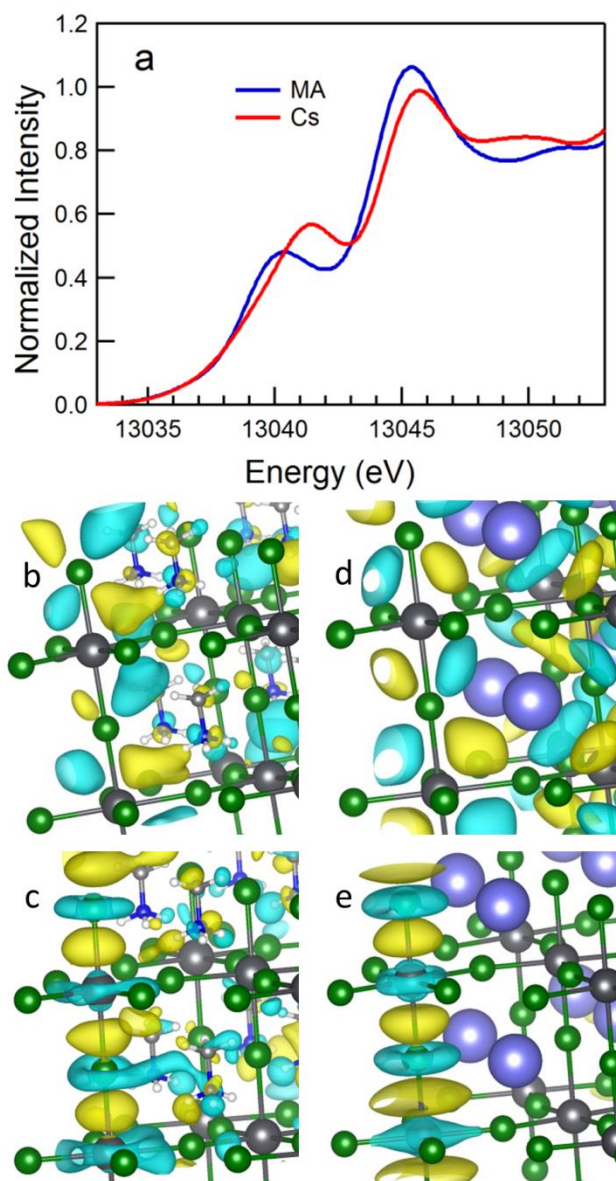


Figure S11: Cation effect. Computed XAS (a) for MAPbI₃ (blue) compared to the same structure with MA replaced by Cs (red). Also shown are edge final state wavefunctions for the strongest transitions in the rising edge (middle) and main edge (bottom) for methylammonium (left column) and Cs (right column). Pb are dark grey, I are green, N are blue, C are light grey, H are white, and Cs are violet. The opposing phases of the orbitals are yellow and cyan.

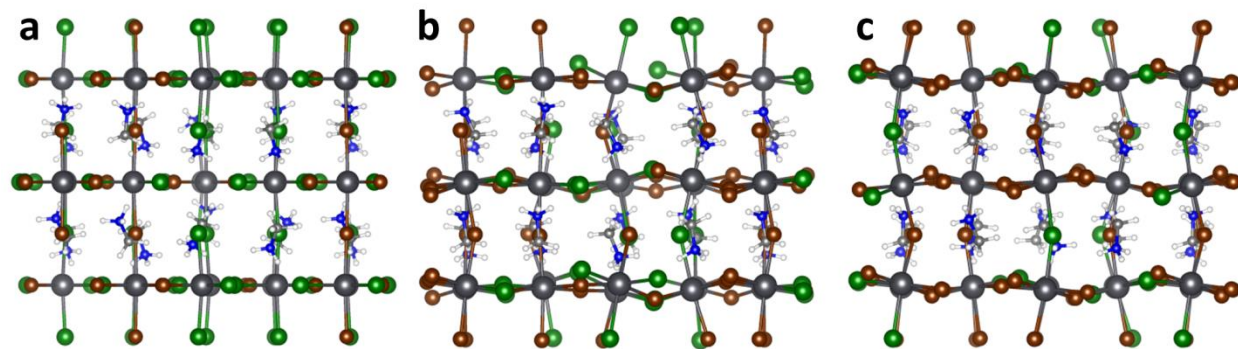


Figure S12: Mixed halide structures. Computed structures for $x = 0.4$, 0.6 and 0.8 (left to right) with randomized distributions of halides. The $x = 0.6$ and $x = 0.8$ structures display a larger degree of octahedral tilting. Pb are dark grey, I are green, Br are brown, N are blue, C are light grey, and H are white.

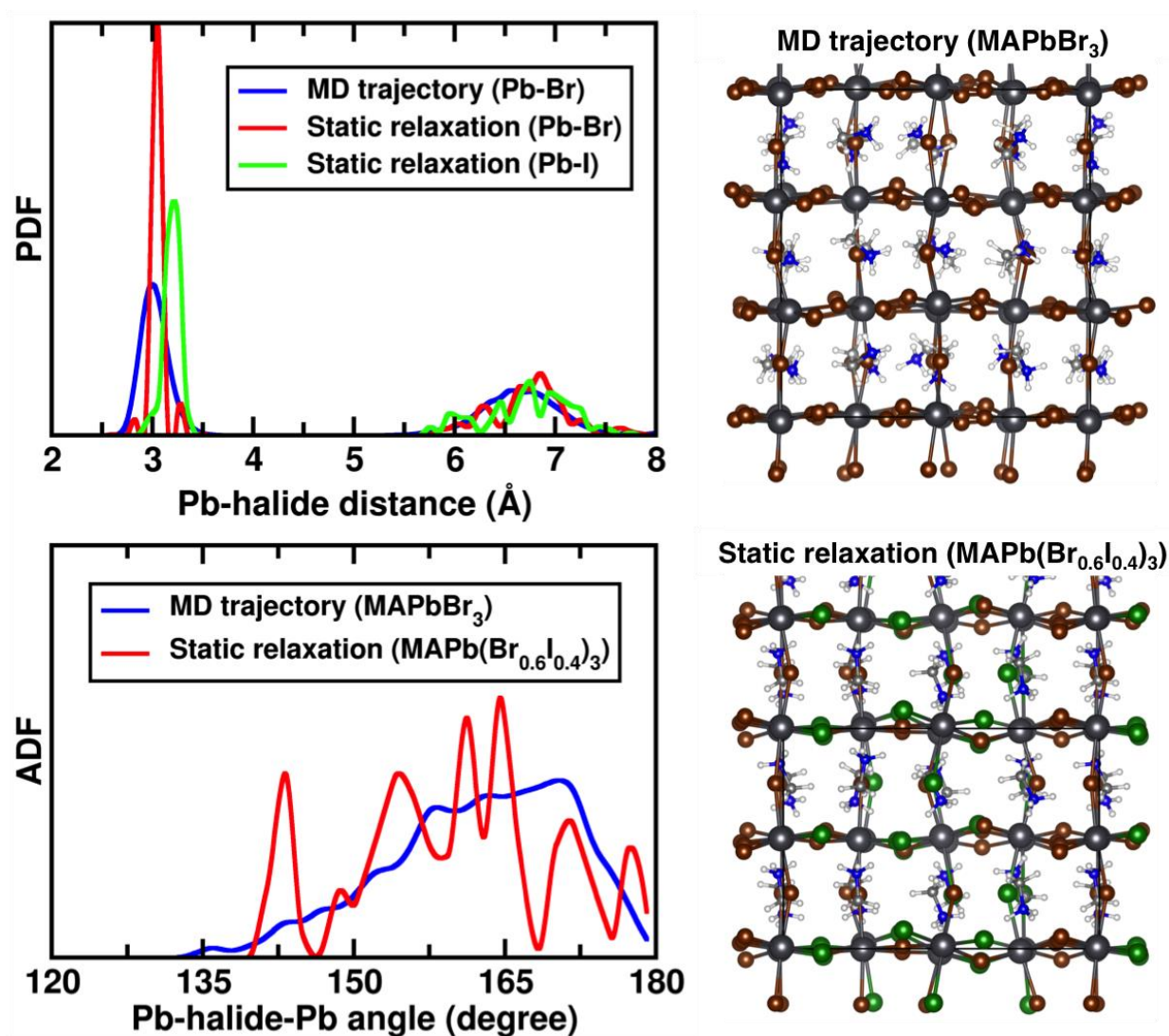


Figure S13: Ab initio MD analysis. Computed pair distribution function (PDF) and angular distribution function (ADF) for room temperature equilibrated MAPbBr_3 and randomized $\text{MAPb}(\text{Br}_{0.6}\text{I}_{0.4})_3$ structure that is optimized at zero temperature. The atomic structures for both MAPbBr_3 (from ab initio molecular dynamics simulation) and $\text{MAPb}(\text{Br}_{0.6}\text{I}_{0.4})_3$ (from 0K relaxation) are visualized on the right. Pb are dark grey, I are green, Br are brown, N are blue, C are light grey, and H are white.

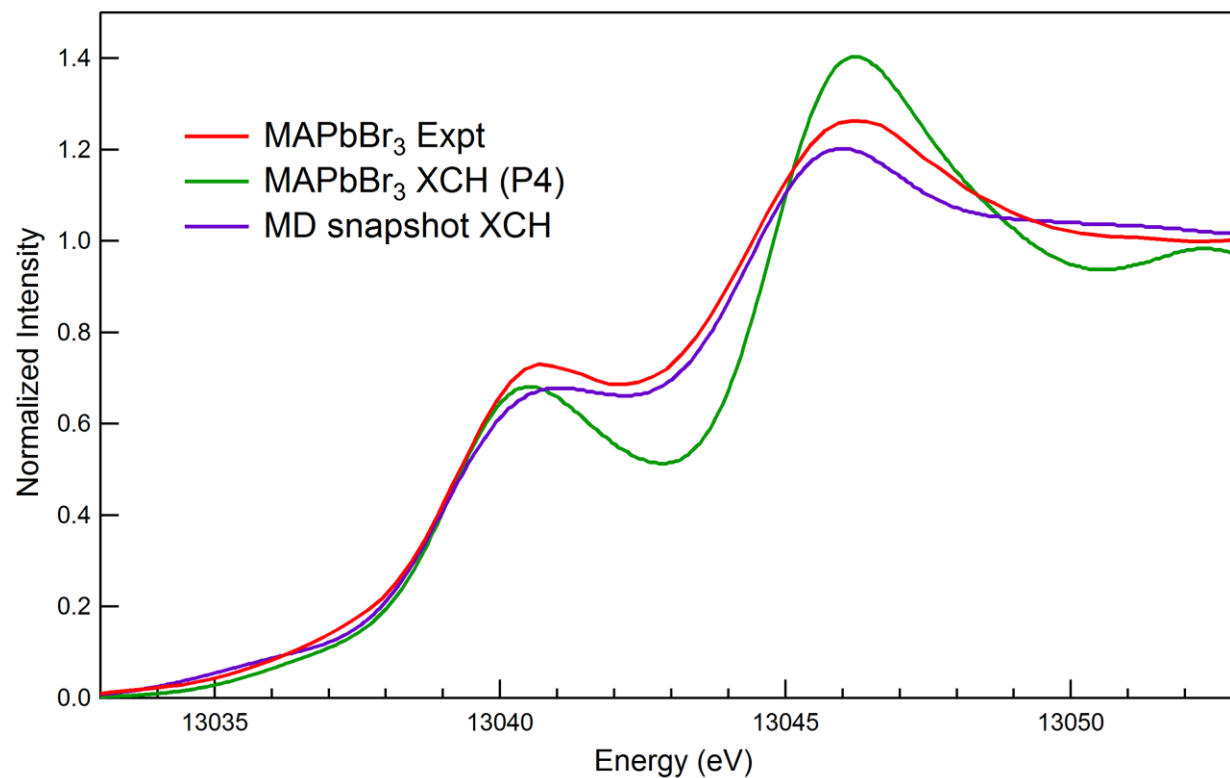


Figure S14: Ab initio MD spectral effect. Calculated XCH spectra for MAPbBr₃ (P4, green), a snapshot structure from the MD run on MAPbBr₃ (purple), and the experimental HERFD XAS spectrum for MAPbBr₃ (red). The MD snapshot captures some of the thermal effects (e.g. octahedral tilts) and better mimics the broadening seen in the experimental spectrum.

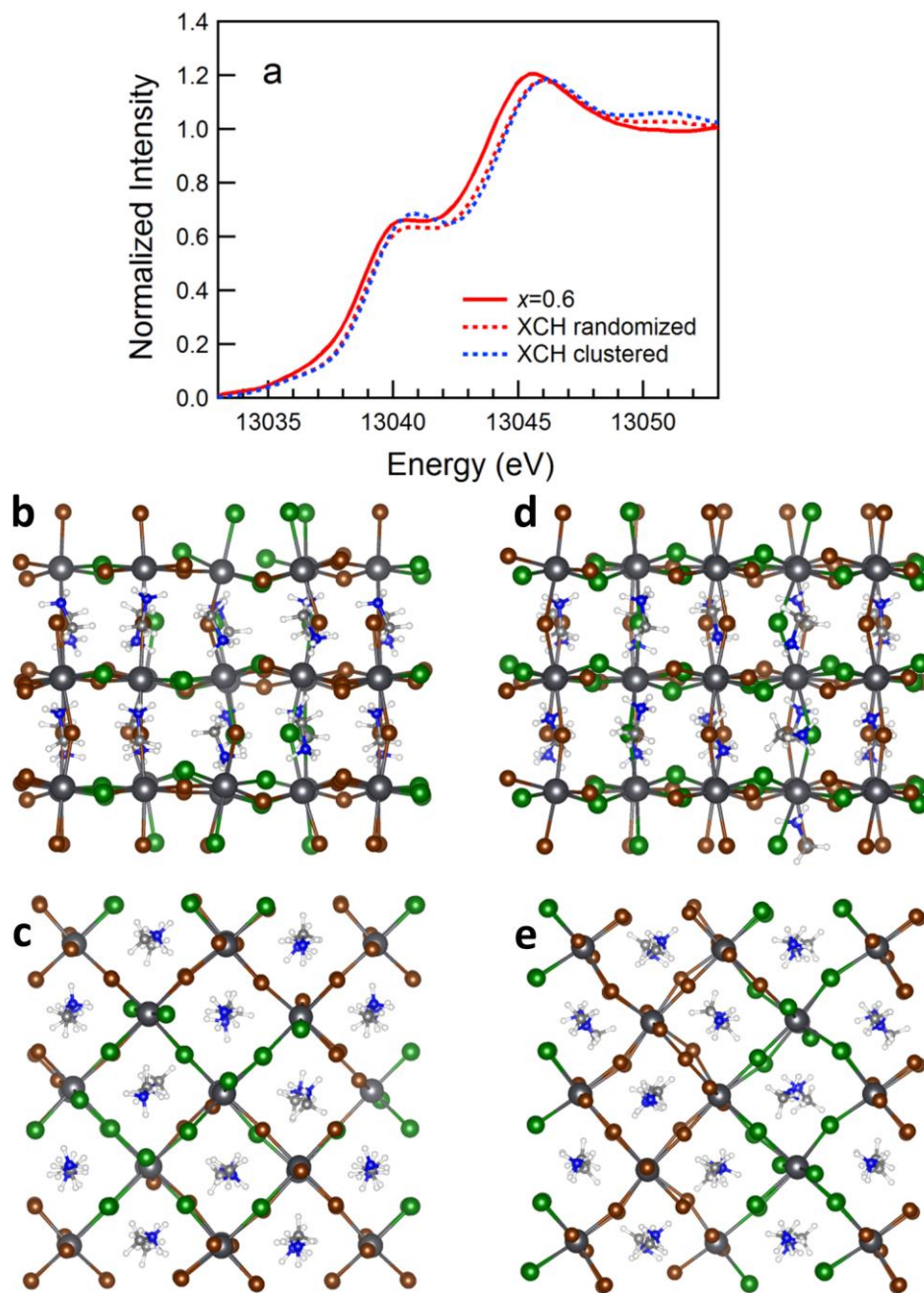


Figure S15: Halide ordering test. (a) Experimental spectrum (red line) for the $x = 0.6$ composition, compared to two calculated spectra. The first (red dashed line) is based on the randomized structure pictured in (b) side view and (c) top view, the second (blue dashed line) is based on the “clustered” structure pictured in (d) side view and (e) top view, in which I and Br are clustered around individual Pb atoms. Pb are dark grey, I are green, Br are brown, N are

blue, C are light grey, and H are white. Both structures display similar degrees of octahedral tilting, and while the calculated spectra are similar, the clustered structure produces a sharpened rising edge feature that does not match experiment. This suggests that the halides are randomly distributed in the actual structure. See Figure S16 for further analysis.

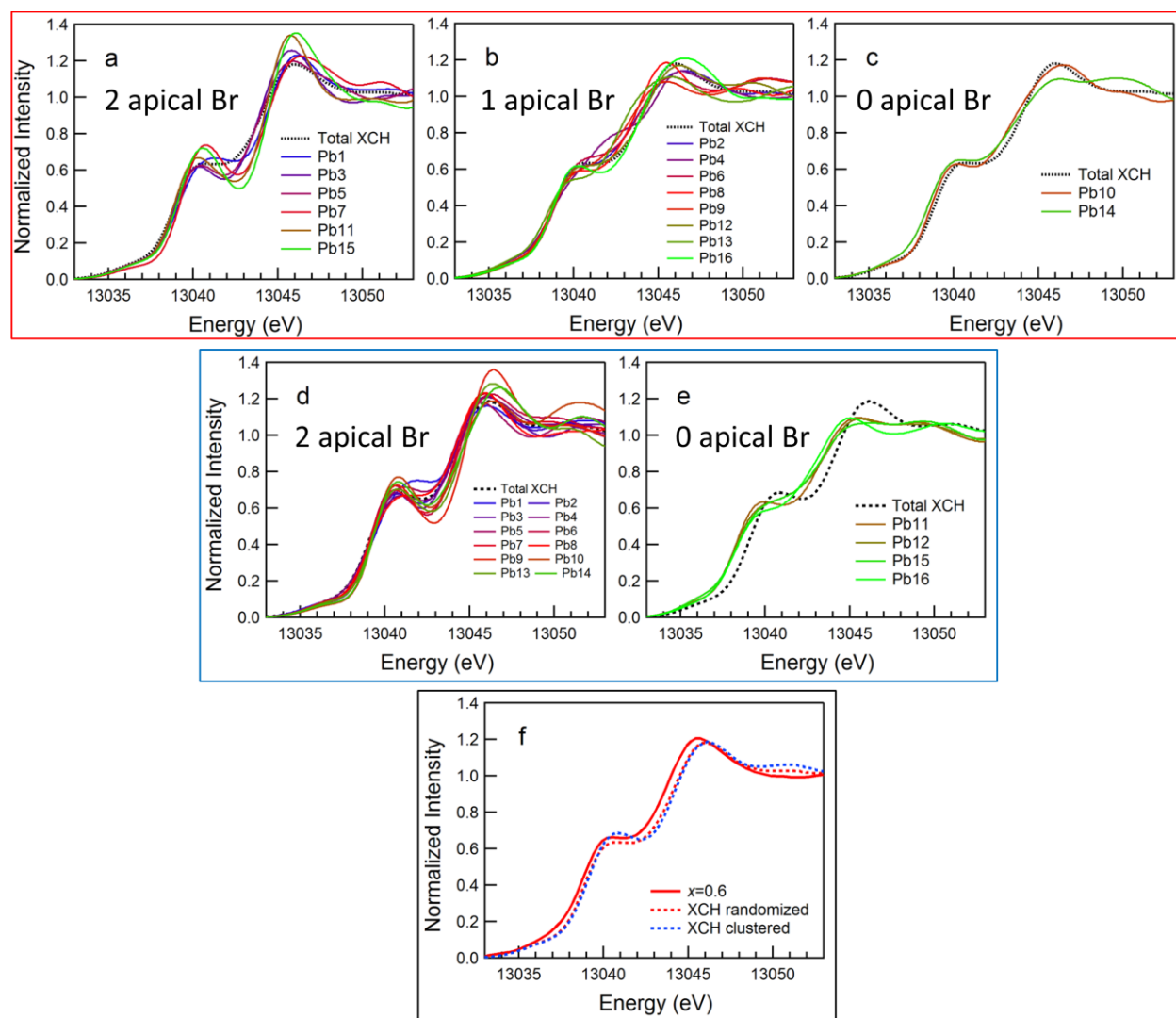


Figure S16: Atom by atom comparison of halide ordering. Top row (red box): individual Pb atom XCH spectra compared to the total average XCH spectrum for the randomized $x = 0.6$ structure, sorted by Pb atoms with (a) 2 apical Br, (b) 1 apical Br, and (c) 0 apical Br, defined as Pb-Br bonds approximately parallel to the orientation of the MA cation. Middle row (blue box): individual Pb atom XCH spectra compared to the total average XCH spectrum for the clustered $x = 0.6$ structure, sorted by Pb atoms with (d) 2 apical Br and (e) 0 apical Br. Bottom row (f): total XCH spectrum for both structures, compared to the experimental spectrum. Spectra for Pb atoms with 2 apical Br generally show a sharper rising edge feature than Pb atoms with 1 or 0

apical Br, and the larger number of these in the clustered structure leads to a slightly sharper rising edge feature in total.

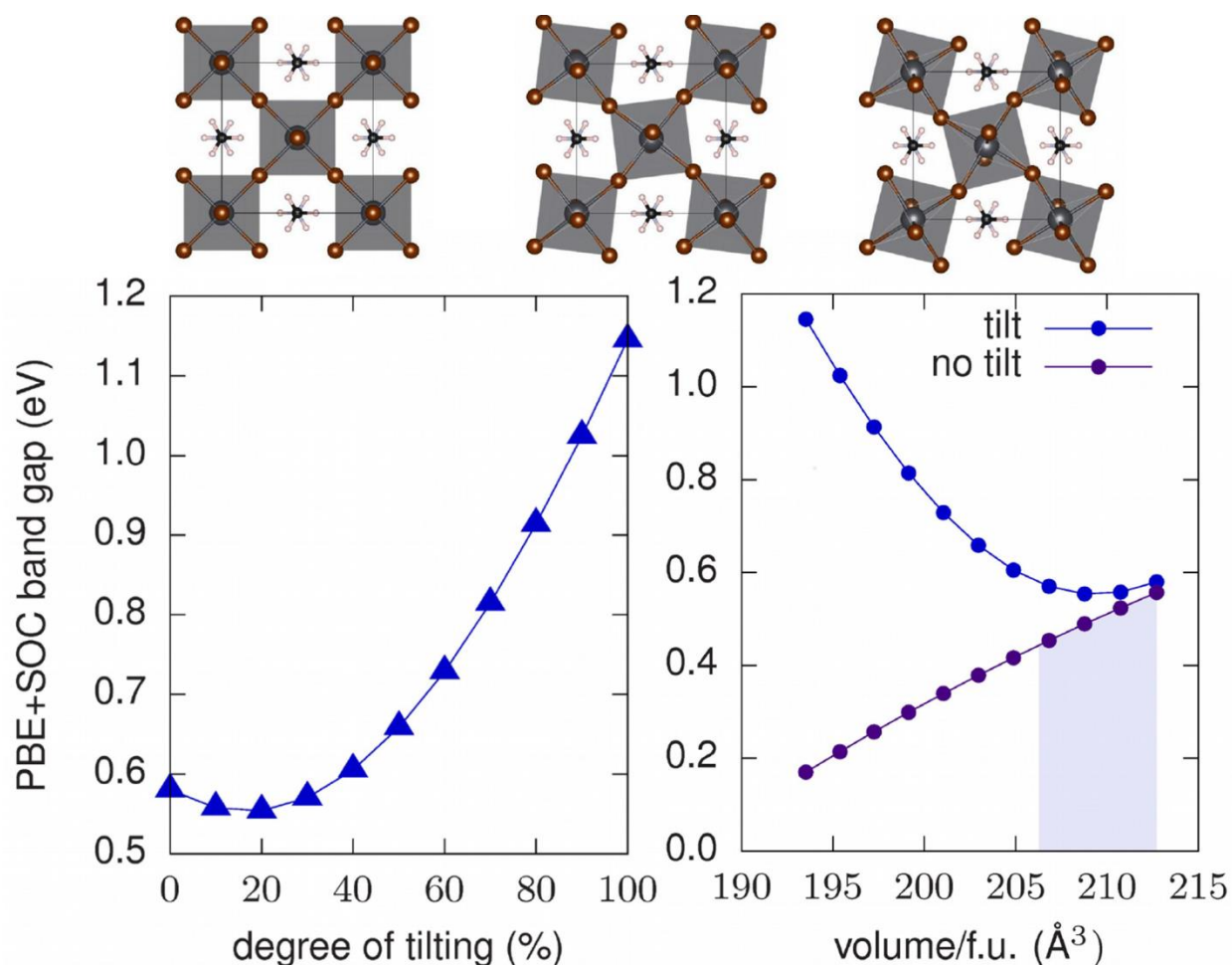


Figure S17: Effect of tilt on band gap. Computed band gaps as a function of degree of octahedral tilting (left panel) between MAPbBr₃ and P5 (~28° tilt). The minimum arises due to the associated changes in lattice parameter and cell volume (right panel). The shaded area corresponds to the range of experimentally reported cell volumes. Pb are dark grey, Br are brown, N are blue, C are light grey, and H are white.

References:

- (1) Hämmäläinen, K.; Siddons, D. P.; Hastings, J. B.; Berman, L. E., Elimination of the inner-shell lifetime broadening in x-ray-absorption spectroscopy. *Phys. Rev. Lett.* **1991**, 67, 2850-2853.

- (2) Carra, P.; Fabrizio, M.; Thole, B. T., High Resolution X-Ray Resonant Raman Scattering. *Phys. Rev. Lett.* **1995**, *74*, 3700-3703.
- (3) Swarbrick, J. C.; Skyllberg, U.; Karlsson, T.; Glatzel, P., High Energy Resolution X-ray Absorption Spectroscopy of Environmentally Relevant Lead(II) Compounds. *Inorg. Chem.* **2009**, *48*, 10748-10756.
- (4) Sokaras, D.; Weng, T.-C.; Nordlund, D.; Alonso-Mori, R.; Velikov, P.; Wenger, D.; Garachtchenko, A.; George, M.; Borzenets, V.; Johnson, B.; Rabedeau, T.; Bergmann, U., A seven-crystal Johann-type hard x-ray spectrometer at the Stanford Synchrotron Radiation Lightsource. *Rev. Sci. Instrum.* **2013**, *84*, 053102.
- (5) Ravel, B.; Newville, M., ATHENA, ARTEMIS, HEPHAESTUS: data analysis for X-ray absorption spectroscopy using IFEFFIT. *J. Synchrotron Radiat.* **2005**, *12*, 537-541.
- (6) Prendergast, D.; Galli, G., X-ray absorption spectra of water from first principles calculations. *Phys. Rev. Lett.* **2006**, *96*, 215502.
- (7) Prendergast, D.; Louie, S. G., Bloch-state-based interpolation: An efficient generalization of the Shirley approach to interpolating electronic structure. *Phys. Rev. B* **2009**, *80*, 235126.
- (8) Giannozzi, P.; Baroni, S.; Bonini, N.; Calandra, M.; Car, R.; Cavazzoni, C.; Ceresoli, D.; Chiarotti, G. L.; Cococcioni, M.; Dabo, I.; Dal Corso, A.; de Gironcoli, S.; Fabris, S.; Fratesi, G.; Gebauer, R.; Gerstmann, U.; Gougoussis, C.; Kokalj, A.; Lazzeri, M.; Martin-Samos, L.; Marzari, N.; Mauri, F.; Mazzarello, R.; Paolini, S.; Pasquarello, A.; Paulatto, L.; Sbraccia, C.; Scandolo, S.; Sclauzero, G.; Seitsonen, A. P.; Smogunov, A.; Umari, P.; Wentzcovitch, R. M., QUANTUM ESPRESSO: a modular and open-source software project for quantum simulations of materials. *J. Phys.: Condens. Matter* **2009**, *21*.
- (9) Taillefumier, M.; Cabaret, D.; Flank, A.-M.; Mauri, F., X-ray absorption near-edge structure calculations with the pseudopotentials: Application to the K edge in diamond and α -quartz. *Phys. Rev. B* **2002**, *66*, 195107.
- (10) Vanderbilt, D., Soft self-consistent pseudopotentials in a generalized eigenvalue formalism. *Phys. Rev. B* **1990**, *41*, 7892-7895.
- (11) Shirley, E. L., Optimal basis sets for detailed Brillouin-zone integrations. *Phys. Rev. B* **1996**, *54*, 16464.
- (12) Hetenyi, B.; De Angelis, F.; Giannozzi, P.; Car, R., Calculation of near-edge x-ray-absorption fine structure at finite temperatures: Spectral signatures of hydrogen bond breaking in liquid water. *J. Chem. Phys.* **2004**, *120*, 8632-8637.
- (13) England, A. H.; Duffin, A. M.; Schwartz, C. P.; Uejio, J. S.; Prendergast, D.; Saykally, R. J., On the hydration and hydrolysis of carbon dioxide. *Chem. Phys. Lett.* **2011**, *514*, 187-195.
- (14) Jiang, P.; Prendergast, D.; Borondics, F.; Porsgaard, S.; Giovanetti, L.; Pach, E.; Newberg, J.; Bluhm, H.; Besenbacher, F.; Salmeron, M., Experimental and theoretical investigation of the electronic structure of Cu₂O and CuO thin films on Cu(110) using x-ray photoelectron and absorption spectroscopy. *J. Chem. Phys.* **2013**, *138*, 024704.
- (15) Becke, A. D., Density - functional thermochemistry. III. The role of exact exchange. *J. Chem. Phys.* **1993**, *98*, 5648-5652.
- (16) Lee, C.; Yang, W.; Parr, R. G., Development of the Colle-Salvetti correlation-energy formula into a functional of the electron density. *Phys. Rev. B* **1988**, *37*, 785.
- (17) Vosko, S. H.; Wilk, L.; Nusair, M., Accurate spin-dependent electron liquid correlation energies for local spin density calculations: a critical analysis. *Can. J. Phys.* **1980**, *58*, 1200-1211.
- (18) Stephens, P. J.; Devlin, F. J.; Chabalowski, C. F.; Frisch, M. J., Ab Initio Calculation of Vibrational Absorption and Circular Dichroism Spectra Using Density Functional Force Fields. *J. Phys. Chem.* **1994**, *98*, 11623-11627.
- (19) Hay, P. J.; Wadt, W. R., Ab initio effective core potentials for molecular calculations. Potentials for K to Au including the outermost core orbitals. *J. Chem. Phys.* **1985**, *82*, 299-310.

- (20) Wadt, W. R.; Hay, P. J., Ab initio effective core potentials for molecular calculations. Potentials for main group elements Na to Bi. *J. Chem. Phys.* **1985**, *82*, 284-298.
- (21) Leguy, A. M. A.; Frost, J. M.; McMahon, A. P.; Sakai, V. G.; Kockelmann, W.; Law, C.; Li, X.; Foglia, F.; Walsh, A.; O'Regan, B. C.; Nelson, J.; Cabral, J. T.; Barnes, P. R. F., The dynamics of methylammonium ions in hybrid organic–inorganic perovskite solar cells. *Nat. Commun.* **2015**, *6*, 7124.
- (22) Blochl, P. E., PROJECTOR AUGMENTED-WAVE METHOD. *Phys. Rev. B* **1994**, *50*, 17953-17979.
- (23) Kresse, G.; Joubert, D., From ultrasoft pseudopotentials to the projector augmented-wave method. *Phys. Rev. B* **1999**, *59*, 1758-1775.
- (24) Kresse, G.; Hafner, J., ABINITIO MOLECULAR-DYNAMICS FOR LIQUID-METALS. *Phys. Rev. B* **1993**, *47*, 558-561.
- (25) Kresse, G.; Furthmüller, J., Efficient iterative schemes for ab initio total-energy calculations using a plane-wave basis set. *Phys. Rev. B* **1996**, *54*, 11169-11186.
- (26) Filippetti, A.; Delugas, P.; Saba, M. I.; Mattoni, A., Entropy-Suppressed Ferroelectricity in Hybrid Lead-Iodide Perovskites. *J. Phys. Chem. Lett.* **2015**, *6*, 4909-4915.
- (27) Bellaiche, L.; Vanderbilt, D., Virtual crystal approximation revisited: Application to dielectric and piezoelectric properties of perovskites. *Phys. Rev. B* **2000**, *61*, 7877-7882.
- (28) Noh, J. H.; Im, S. H.; Heo, J. H.; Mandal, T. N.; Seok, S. I., Chemical Management for Colorful, Efficient, and Stable Inorganic–Organic Hybrid Nanostructured Solar Cells. *Nano Lett.* **2013**, *13*, 1764-1769.
- (29) Kawamura, Y.; Mashiyama, H.; Hasebe, K., Structural Study on Cubic–Tetragonal Transition of $\text{CH}_3\text{NH}_3\text{PbI}_3$. *J. Phys. Soc. Jpn.* **2002**, *71*, 1694-1697.
- (30) Egger, D. A.; Kronik, L., Role of Dispersive Interactions in Determining Structural Properties of Organic–Inorganic Halide Perovskites: Insights from First-Principles Calculations. *J. Phys. Chem. Lett.* **2014**, *5*, 2728-2733.
- (31) Lee, J.-H.; Bristowe, N. C.; Bristowe, P. D.; Cheetham, A. K., Role of hydrogen-bonding and its interplay with octahedral tilting in $\text{CH}_3\text{NH}_3\text{PbI}_3$. *Chem. Commun.* **2015**, *51*, 6434-6437.